

The accuracy of post-processing nucleosynthesis

Eduardo Bravo[★]

E.T.S. Arquitectura del Vallès, Universitat Politècnica de Catalunya, Carrer Pere Serra 1-15, 08173 Sant Cugat del Vallès, Spain

Accepted XXX. Received YYY; in original form ZZZ

ABSTRACT

The computational requirements posed by multi-dimensional simulations of type Ia supernovae make it difficult to incorporate complex nuclear networks to follow the release of nuclear energy along with the propagation of the flame. Instead, these codes usually model the flame and use simplified nuclear kinetics with the goal to determine a sufficiently accurate rate of nuclear energy generation and, afterwards, post-process the thermodynamic trajectories with a large nuclear network to obtain more reliable nuclear yields. In this work, I study the performance of simplified nuclear networks with respect to the reproduction of the correct nuclear yields. The first point I address is the definition of a strategy to follow the properties of matter in nuclear statistical equilibrium (NSE). I propose that the best approach is to use published tables of NSE properties together with a careful interpolation routine. Second, I test several simplified nuclear networks for the accuracy of the nucleosynthesis obtained through post-processing, compared with the nucleosynthesis resulting directly from a one-dimensional supernova code equipped with a large nuclear network. Short networks (iso7 and 13 α) are able to give an accurate yield of ⁵⁶Ni, after post-processing, but can fail by order of magnitude predicting the ejected mass of even mildly abundant species ($> 10^{-3} M_{\odot}$). A network of 21 species reproduces the nucleosynthesis of Chandrasekhar and sub-Chandrasekhar explosions with average errors better than 20% for the whole set of stable elements and isotopes followed in the model.

Key words: nuclear reactions, nucleosynthesis, abundances – supernovae: general – white dwarfs

1 INTRODUCTION

Type Ia supernovae (SNIa) are the result of the thermonuclear disruption of carbon-oxygen white dwarf (WD) stars, which results from their destabilization by a companion star in a binary or a ternary system (Hillebrandt & Niemeyer 2000; Howell 2011; Katz & Dong 2012; Maoz et al. 2014). The spectra and light curves of SNIa can be recorded starting shortly after the explosion (Zheng et al. 2013; Hosseinzadeh et al. 2017; Miller et al. 2018) and until a few years later (Graur et al. 2018; Jacobson-Galán et al. 2018; Maguire et al. 2018), if the luminosity and the distance to the event allow it. Besides providing valuable insights into the systematics of SNIa (Branch et al. 1993; Filippenko 1997; Poznanski et al. 2002; Howell et al. 2005; James et al. 2006; Arsenijevic et al. 2008; Branch et al. 2009, to only cite a few), these data allow constraining the properties of the explosion, from fundamental parameters, such as the ejected mass, explosion energy, and synthesized mass of ⁵⁶Ni (Stritzinger et al. 2006; Scalzo et al. 2014), to second-order details, such as the ejected amounts of other radioactive isotopes, notably ⁵⁷Ni

and ⁵⁵Fe (Graur et al. 2016; Dimitriadis et al. 2017; Shappee et al. 2017; Yang et al. 2018; Li et al. 2019). Whereas observational data are usually reported together with their error bars, there is scarce knowledge of the effects of the diverse sources of uncertainty related to supernova models. Indeed, Bravo & Martínez-Pinedo (2012); Parikh et al. (2013); Bravo (2019) proved that the nucleosynthesis of one-dimensional SNIa models is robust with respect to variations in individual reaction rates, at least during the explosion phase.

Currently, two competing models may account for the bulk of SNIa. In one model, the exploding WD is close to the Chandrasekhar-mass limit and the disruption is total, therefore, the mass of the ejecta is fixed a priori. The most accepted explosion mechanism of massive WDs is a delayed detonation (DDT, Khokhlov 1991), in which the thermonuclear burning wave propagates subsonically at first and turns into a detonation later, typically one or two seconds after thermal runaway. In the other model, the mass of the exploding WD is substantially less than the Chandrasekhar limit, the burning wave propagates as a detonation from the very beginning, and the instability leading to the detonation may be a consequence of the burning of a thin helium layer, accumulated on top of the WD after accretion from a

[★] E-mail: eduardo.bravo@upc.edu

secondary star, or it may be due to the merging or collision with another degenerate star (e.g. a second WD; Woosley & Weaver 1994; Woosley & Kasen 2010; Sim et al. 2010; Kushnir et al. 2013).

Although there is not consensus about the level of asymmetry involved in SNIa explosions, most polarization measurements are indicative of small deviations from spherical symmetry (Wang et al. 1996; Howell et al. 2001; Maund et al. 2010; Maeda et al. 2010a; Maund et al. 2013). One-dimensional models are able to account for the properties of SNIa in the visible (Höflich & Khokhlov 1996; Nugent et al. 1997; Tanaka et al. 2011; Blondin et al. 2013; Höflich et al. 2017) and gamma bands (Churazov et al. 2014, 2015, see Diehl et al. 2014; Isern et al. 2016 for a different view), and those of their remnants in the X-ray and radio bands (e.g. Badenes et al. 2006; Lopez et al. 2011; Martínez-Rodríguez et al. 2018). However, to understand SNIa it is necessary to simulate the explosion in three dimensions, either to account for hydrodynamical instabilities and turbulence (e.g. Plewa et al. 2004; Röpke et al. 2006; Bravo & García-Senz 2006; Kasen & Woosley 2007), or to address the inherent asymmetrical configuration of colliding or merging WDs.

The computational requirements posed by three-dimensional hydrodynamics make it difficult incorporating complex nuclear networks to follow the release of nuclear energy along with the propagation of the flame. Usually, multi-dimensional supernova codes need to model the flame making use of simplified nuclear kinetics with the goals to give an accurate rate of nuclear energy generation and compute the explosion in a reasonable time. Afterwards, the thermodynamic trajectories of the integration nodes can be post-processed with the aid of a large nuclear network to obtain more reliable values of the supernova yields (e.g. Thielemann et al. 1986; Bravo et al. 2010; Townsley et al. 2016; Leung & Nomoto 2017).

In this work, I address the question of the performance of simplified nuclear networks with respect to the reproduction of the correct nuclear yields¹. After a brief explanation of the methodology used (Sect. 2), the first point I treat is the definition of a strategy to follow the properties of matter in a state of nuclear statistical equilibrium (NSE, Sect. 3). In the next section, I test several simplified nuclear networks for the accuracy of the nucleosynthesis obtained through post-processing (Sect. 4). Two more sections address the performance of simplified nuclear networks for high-metallicity WD progenitors and the effect of different criteria for switching on and off NSE routines. A final section is dedicated to the conclusions of the present work.

2 METHODOLOGY

The simulations presented in this work are performed with the same supernova code described in Bravo et al. (2019), where extensive details of the method of computation can be found. The code integrates the hydrodynamic evolution using a large nuclear network, solves the Saha equations

¹ In the present work, by correct nuclear yields I mean those obtained with the same supernova code without the simplifications described in the text.

for NSE, when applicable, and calculates the neutronization rate and associated neutrino energy losses at each time step, computing the weak interaction rates on the NSE composition. The hydrodynamics is followed in one dimension, assuming spherical symmetry, but the nucleosynthetic processes through which matter passes are the same as in any three-dimensional SNIa simulation, hence, it is appropriate to assess the accuracy of the computed nucleosynthesis. Furthermore, the supernova models generated by this code have been successfully compared with observed optical spectra (S. Blondin, private communication), gamma-ray emission from SN2014J (Churazov et al. 2014, 2015; Isern et al. 2016), and the X-ray spectra of supernova remnants (Badenes et al. 2006).

The default nuclear network used here is the same as in Bravo & Martínez-Pinedo (2012), as given in column BM-P in Table 1. This network includes all stable isotopes up to molybdenum, but the code allows to define different nuclear networks by simply listing the species to be followed. The nuclear reactions linking these species are included automatically in the network, together with a basic set formed by the fusion reactions triple- α , $^{12}\text{C}+^{12}\text{C}$, $^{16}\text{O}+^{16}\text{O}$, and $^{12}\text{C}+^{16}\text{O}$. All reaction rates are taken from the JINA REACLIB compilation (Cyburt et al. 2010). For some of the tests addressed later, it has been necessary to adapt the code to change some rates or in other ways that are described in Sect. 4.

As references, I have selected two explosion models suitable for normal-luminosity SNIa, characterized by an ejected mass of ^{56}Ni about $M(^{56}\text{Ni}) \sim 0.5 - 0.7 M_{\odot}$. The first model, sub- M_{Ch} , is a central detonation of a sub-Chandrasekhar WD of mass $M_{\text{WD}} = 1.06 M_{\odot}$ (model 1p06_Z9e-3_std in Bravo et al. 2019). The second one, M_{Ch} , is a delayed detonation of a massive WD with central density $\rho_c = 3 \times 10^9 \text{ g cm}^{-3}$ and a deflagration-to-detonation transition density $\rho_{\text{DDT}} = 2.4 \times 10^7 \text{ g cm}^{-3}$ (model ddt2p4_Z9e-3_std in Bravo et al. 2019). Both models assume an initial composition made of equal masses of ^{12}C and ^{16}O , contaminated with ^{22}Ne as appropriate for progenitor metallicity 0.009, and other metals from sodium to indium in solar proportions with respect to ^{22}Ne .

To assess the accuracy of the nucleosynthetic yields I use a set of fourteen indicators, all of them expressed as percent relative differences between the quantities obtained in a test model with respect to the results in the reference hydrodynamic model that uses the default reaction network. Therefore, I compare sub-Chandrasekhar models to model 1p06_Z9e-3_std, and Chandrasekhar-mass models to ddt2p4_Z9e-3_std. The indicators are:

- the discrepancy of the final kinetic energy, $i_1 = \Delta K/K$,
- the discrepancy of the ejected mass of ^{56}Ni , $i_2 = \Delta M(^{56}\text{Ni})/M(^{56}\text{Ni})$,
- the discrepancy of the ejected mass of ^{57}Ni , $i_3 = \Delta M(^{57}\text{Ni})/M(^{57}\text{Ni})$,
- the discrepancy of the ejected mass of ^{55}Fe , $i_4 = \Delta M(^{55}\text{Fe})/M(^{55}\text{Fe})$,
- a measure of the discrepancy based on the average of the squared deviations of the logarithm of the ejected mass

Table 1. Nuclear networks for the convergence study.

Z	BM-P	netAKh	nse7
	$A_{\min} - A_{\max}$	$A_{\min} - A_{\max}$	$A_{\min} - A_{\max}$
n	1 - 1	1 - 1	1 - 1
H	1 - 4	1 - 1	1 - 3
He	3 - 9	4 - 4	3 - 6
Li	4 - 11	-	6 - 7
Be	6 - 14	-	7 - 10
B	7 - 17	-	10 - 11
C	8 - 20	12 - 13	11 - 14
N	10 - 21	13 - 13	13 - 15
O	12 - 23	16 - 16	15 - 18
F	14 - 25	-	17 - 19
Ne	16 - 27	20 - 22	19 - 23
Na	18 - 34	23 - 23	21 - 25
Mg	20 - 35	23 - 26	23 - 28
Al	22 - 36	27 - 27	25 - 30
Si	24 - 38	27 - 32	27 - 33
P	26 - 40	30 - 33	29 - 35
S	28 - 42	31 - 36	30 - 37
Cl	30 - 44	35 - 37	32 - 39
Ar	32 - 46	36 - 41	34 - 42
K	34 - 49	39 - 43	37 - 45
Ca	36 - 51	40 - 46	38 - 48
Sc	38 - 52	41 - 47	41 - 51
Ti	40 - 54	43 - 50	43 - 53
V	42 - 56	45 - 52	45 - 55
Cr	44 - 58	47 - 56	47 - 57
Mn	46 - 60	49 - 60	49 - 59
Fe	49 - 63	51 - 62	50 - 62
Co	51 - 65	53 - 61	52 - 64
Ni	53 - 69	56 - 64	54 - 66
Cu	55 - 71	57 - 65	56 - 68
Zn	57 - 78	59 - 66	58 - 70
Ga	61 - 81	-	61 - 72
Ge	63 - 83	-	64 - 74
As	65 - 85	-	69 - 75
Se	67 - 87	-	75 - 75
Br	69 - 90	-	-
Kr	71 - 93	-	-
Rb	73 - 99	-	-
Sr	77 - 100	-	-
Y	79 - 101	-	-
Zr	81 - 101	-	-
Nb	85 - 101	-	-
Mo	87 - 101	-	-
Tc	89 - 101	-	-
Ru	91 - 101	-	-
Rh	93 - 101	-	-
Pd	95 - 101	-	-
Ag	97 - 101	-	-
Cd	99 - 101	-	-
In	101 - 101	-	-

of the elements,

$$\sigma_{\log, \text{ele}} = \sqrt{\frac{1}{N_{\text{ele}}} \sum \log^2 \left[\frac{M'(Z)}{M(Z)} \right]}, \quad (1)$$

$$i_5 = 10^{\sigma_{\log, \text{ele}}} - 1, \quad (2)$$

• a measure of the discrepancy based on the average of the squared deviations of the logarithm of the ejected mass

of the isotopes,

$$\sigma_{\log, \text{iso}} = \sqrt{\frac{1}{N_{\text{iso}}} \sum \log^2 \left[\frac{M'(A_Z)}{M(A_Z)} \right]}, \quad (3)$$

$$i_6 = 10^{\sigma_{\log, \text{iso}}} - 1, \quad (4)$$

• a measure of the discrepancy based on a weighted average of the squared deviations of the logarithm of the ejected mass of the elements,

$$\sigma_{\text{wm, ele}} = \sqrt{\sum \omega(Z) \log^2 \left[\frac{M'(Z)}{M(Z)} \right]}, \quad (5)$$

$$i_7 = 10^{\sigma_{\text{wm, ele}}} - 1, \quad (6)$$

• a measure of the discrepancy based on a weighted average of the squared deviations of the logarithm of the ejected mass of the isotopes,

$$\sigma_{\text{wm, iso}} = \sqrt{\sum \omega(A_Z) \log^2 \left[\frac{M'(A_Z)}{M(A_Z)} \right]}, \quad (7)$$

$$i_8 = 10^{\sigma_{\text{wm, iso}}} - 1, \quad (8)$$

• the maximum relative discrepancy, i_9 , in the mass of the elements whose final yield is $M(Z) \geq 10^{-3} M_{\odot}$,

• the maximum relative discrepancy, i_{10} , in the mass of the elements whose final yield lies in the range $10^{-3} > M(Z) \geq 10^{-6} M_{\odot}$,

• the maximum relative discrepancy, i_{11} , in the mass of the elements whose final yield lies in the range $10^{-6} > M(Z) \geq 10^{-12} M_{\odot}$,

• the maximum relative discrepancy, i_{12} , in the mass of the isotopes whose final yield is $M(A_Z) \geq 10^{-3} M_{\odot}$,

• the maximum relative discrepancy, i_{13} , in the mass of the isotopes whose final yield lies in the range $10^{-3} > M(A_Z) \geq 10^{-6} M_{\odot}$, and

• the maximum relative discrepancy, i_{14} , in the mass of the isotopes whose final yield lies in the range $10^{-6} > M(A_Z) \geq 10^{-12} M_{\odot}$.

The quantities $M(Z)$ and $M(A_Z)$ are the masses, in M_{\odot} , of element Z and isotope A_Z in the reference model, M' stand for the same quantities for the test model, N_{ele} and N_{iso} are, respectively the number of different elements and isotopes ejected, and the weighting functions are defined as:

$$\omega(Z) = \frac{1}{\left[\log^2 M(Z) \right] \times \sum \left[1 / \log^2 M(Z) \right]}, \quad (9)$$

$$\omega(A_Z) = \frac{1}{\left[\log^2 M(A_Z) \right] \times \sum \left[1 / \log^2 M(A_Z) \right]}. \quad (10)$$

With these definitions, indicators i_7 and i_8 provide a measure of the mean deviation of the most abundant species, while indicators i_5 and i_6 give a measure of the deviation of the yields of all species. Indicators i_2 , i_3 , and i_4 are evaluated from the ejected masses of the isotopes 100 s after thermal runaway. All the indicators from i_5 to i_{14} refer to the elemental or isotopic yields of isotopes between carbon and krypton after radioactive decays.

For reference, the kinetic energy and masses of radioactive isotopes ejected in the two reference models are the

Table 2. Nucleosynthetic indicators.

		i_1	i_2	i_3	i_4	i_5	i_6	i_7	i_8	i_9	i_{10}	i_{11}	i_{12}	i_{13}	i_{14}
		(%)	(%)	(%)	(%)	(%)	(%)	(%)	(%)	(%)	(%)	(%)	(%)	(%)	(%)
Convergence study															
Network	Model														
netAKh	M_{Ch}	0.3	0.3	1.0	0.2	3.0	4.9	0.5	0.9	2.2	8.9	9.8	2.2	8.4	35
nse7	M_{Ch}	0.0	0.1	0.6	0.1	4.0	5.4	0.4	0.9	0.9	15	12	1.0	14	35
netAKh	sub- M_{Ch}	0.3	0.1	0.5	0.9	4.1	4.6	0.6	1.0	3.1	19	14	3.1	19	37
nse7	sub- M_{Ch}	0.0	0.1	0.2	0.6	4.2	4.7	0.6	1.0	1.8	19	14	1.8	19	38
NSE table interpolation															
Interpolator	Model														
linlog	M_{Ch}	0.2	0.6	11	7.6	4.3	23	0.9	4.4	7.4	12	0.8	22	100	360
linlin	M_{Ch}	0.0	0.0	0.1	0.0	1.0	8.3	0.2	1.5	0.9	4.7	0.3	8.2	32	82
loglog	M_{Ch}	0.2	0.6	13	7.1	4.3	23	0.9	4.4	7.4	12	0.8	22	101	355
poly	M_{Ch}	0.1	0.5	13	7.4	4.8	28	0.9	5.0	7.9	13	1.9	24	120	490
spline	M_{Ch}	0.0	0.0	0.1	0.0	0.1	0.2	0.0	0.1	0.1	0.2	0.4	0.6	0.7	0.8
pevn	M_{Ch}	0.0	0.1	0.3	0.1	0.2	0.6	0.1	0.1	0.3	0.3	1.4	0.8	1.1	4.2
Simplified networks															
Network	Model														
iso7	M_{Ch}	0.5	9.3	84	29	58	120	12	23	63	620	22	310	1500	5700
13 α	M_{Ch}	3.7	4.2	69	27	43	95	7.2	17	49	380	17	220	920	3000
net21	M_{Ch}	4.3	3.3	5.8	6.4	11	11	3.6	4.3	17	24	23	17	24	38
net23	M_{Ch}	4.5	3.3	9.3	8.6	9.9	10	3.6	4.3	15	21	22	15	20	39
iso7	sub- M_{Ch}	0.8	6.0	26	30	33	46	11	15	52	140	14	92	170	400
13 α	sub- M_{Ch}	1.2	3.8	20	26	24	33	7.4	11	39	93	11	66	110	240
net21	sub- M_{Ch}	1.4	1.2	0.2	1.9	4.2	5.3	1.6	1.9	6.9	10	18	6.9	10	32
net23	sub- M_{Ch}	1.4	0.5	1.4	3.0	4.4	5.9	1.0	1.5	3.7	15	16	4.3	14	35
High metallicity progenitor															
Network	Model														
net21	M_{Ch}	3.8	4.6	13	5.5	11	14	3.8	7.6	20	19	9.9	23	21	65
net23	M_{Ch}	6.0	2.6	2.2	8.1	15	17	4.2	7.6	29	29	15	29	69	66
net21	sub- M_{Ch}	2.4	5.9	9.6	6.6	15	18	6.9	9.9	20	30	20	27	31	22
net23	sub- M_{Ch}	2.9	0.2	0.9	4.1	6.3	7.2	1.8	3.3	7.7	12	13	12	14	53
Transition NSE \leftrightarrow net21															
Condition	Model														
$T_{\text{NSE}} = 5.5 \times 10^9$ K	M_{Ch}	4.3	3.3	5.8	6.4	11	11	3.6	4.3	17	24	23	17	24	38
$T_{\text{NSE}} = 5.0 \times 10^9$ K	M_{Ch}	3.5	1.7	9.5	6.9	7.7	8.5	2.1	2.8	8.4	24	18	8.8	23	37
$T_{\text{out}} = 4 \times 10^9$ K	M_{Ch}	3.3	0.6	13	7.9	6.4	8.2	1.3	2.2	8.9	19	15	12	25	36
$T_{\text{out}} = 3 \times 10^9$ K	M_{Ch}	3.3	1.2	2.0	1.5	19	40	2.9	8.9	20	99	17	68	260	490
$\rho_{\text{NSE0}} = 10^8$ g cm $^{-3}$	M_{Ch}	4.4	3.5	3.5	4.5	10	10	3.7	4.4	18	22	23	18	22	38
$\rho_{\text{NSE0}} = 4 \times 10^7$ g cm $^{-3}$	M_{Ch}	4.3	3.3	6.0	6.2	10	11	3.6	4.4	17	20	23	18	20	38

following: in model ddt2p4_Z9e-3_std, $K = 1.42 \times 10^{51}$ erg, $M(^{56}\text{Ni}) = 0.685 M_{\odot}$, $M(^{57}\text{Ni}) = 7.15 \times 10^{-3} M_{\odot}$, and $M(^{55}\text{Fe}) = 9.65 \times 10^{-3} M_{\odot}$; in model 1p06_Z9e-3_std, $K = 1.32 \times 10^{51}$ erg, $M(^{56}\text{Ni}) = 0.664 M_{\odot}$, $M(^{57}\text{Ni}) = 1.01 \times 10^{-2} M_{\odot}$, and $M(^{55}\text{Fe}) = 3.21 \times 10^{-3} M_{\odot}$.

As a first test of convergence of the supernova code with respect to the size of the nuclear network, I have re-computed models M_{Ch} and sub- M_{Ch} with two different nuclear networks, both of them sufficiently large to give accurate nuclear energy generation-rates. The first network (netAKh) is that employed in the SNIa models computed by Alexei Khokhlov and reported in [Blondin et al. \(2013, 2017\)](#). It uses 144 isotopes, including all stable isotopes between neon and copper with the exception of ^{48}Ca . The second network (nse7) includes 260 isotopes and was introduced by [Kushnir \(2019\)](#) and used in their study of the structure of detonation waves in SNIa. It includes all stable isotopes up to arsenic with the exception of ^{76}Ge . Table 1 shows both networks.

The thermodynamic trajectories obtained with the ne-

tAKh and nse7 networks have been fed to a post-processing nuclear code that uses the same network and reaction rates as in the BM-P network². Table 2 show the results in the rows under the header ‘‘Convergence study’’. The agreement with the results of the hydrodynamic calculation using the default network is very satisfactory. The direct measure of the nuclear energy released, that is the final kinetic energy, is reproduced in all four calculations to better than 0.3%. The yields of the radioactive isotopes are reproduced to within 1% with both networks and, in particular, the yield of ^{56}Ni to better than 0.3%.

The nucleosynthesis of stable isotopes and elements also converges, where both netAKh and nse7 obtain similar ratios. The mean deviation of the most abundant elements and isotopes is within 0.4-1%, while that representative of all ejected species is approximately 3-5%. Finally, the maxi-

² The same strategy has been applied to all the calculations presented in the following sections.

mum deviation of elements and isotopes whose yield is larger than $10^{-3} M_{\odot}$ is within 1-3%, that of elements and isotopes with yields between $10^{-3} M_{\odot}$ and $10^{-6} M_{\odot}$ is about 8-19%, and that of the less abundant elements and isotopes is less than 40%.

3 NUCLEAR STATISTICAL EQUILIBRIUM

One of the key ingredients of simulations of SNIa explosions is the treatment of NSE in matter burnt at high density. The composition of matter in NSE can be calculated solving a set of Saha equilibrium equations linking the abundances of all isotopes to two arbitrarily chosen abundances (or combinations thereof), which play the role of independent variables, plus two closure relationships that account for the conservation of baryon number and the electrical neutrality of matter. The procedure is usually iterative, which makes it inefficient for a multi-dimensional hydrodynamic computation of a supernova explosion. Therefore, in this sort of simulations, it is usual to rely on interpolation on a table of NSE states, pre-computed on a net of density, ρ , temperature, T , and electron mole number, Y_e , nodes, the denser the better. Usually, the table gives the main properties of matter in NSE, including nuclear binding energy, mean molar number, neutronization rate, and neutrino energy loss rate.

One example of this kind of tables of NSE properties is given in [Seitenzahl et al. \(2009\)](#). Recently, [Bravo et al. \(2019\)](#) reported that the final yields computed using their NSE table might disagree by order of magnitude for some isotopes with respect to those obtained computing the NSE state properties on the fly in the hydrodynamical calculation. The discrepancy did not affect significantly either the total energy release, that is the final kinetic energy, or the ejected mass of ^{56}Ni , and was attributed to the interpolation procedure applied to obtain the NSE properties out of the ρ , T , and Y_e table nodes.

Here, I argue that the culprit of the just mentioned discrepancy relies on the interpolation on the density nodes. To illustrate the situation, Fig. 1 shows the neutrino energy loss-rate, ε_{ν} , in a sample of the [Seitenzahl et al. \(2009\)](#) table nodes of ρ , T , and Y_e for typical values during the supernova explosion. While the energy loss rate changes smoothly between consecutive temperature and electron mole number nodes, the dependence on density is more complex and the values of ε_{ν} change by four orders of magnitude between ρ node numbers 12 and 20 ($\rho = 2 \times 10^8 \text{ g cm}^{-3}$ and $\rho = 2 \times 10^{10} \text{ g cm}^{-3}$). This huge change makes the results of the interpolation in density sensitive to the interpolation procedure. Indeed, the plot of ε_{ν} versus density in between nodes 12 and 20 in Fig. 1 is suggestive of a linear dependence between $\log \varepsilon_{\nu}$ and $\log \rho$ (the table nodes are equispaced in $\log \rho$).

To test the impact of the NSE table interpolation scheme I have chosen different interpolants and computed the difference in NSE properties with respect to those obtained by solving the NSE Saha equilibrium equations. The interpolants used and the designations given are the following:

- linear interpolation of NSE properties, for example ε_{ν} or the neutronization rate \dot{Y}_e , with respect to $\log \rho$ (linlog),
- linear interpolation with respect to ρ (linlin),

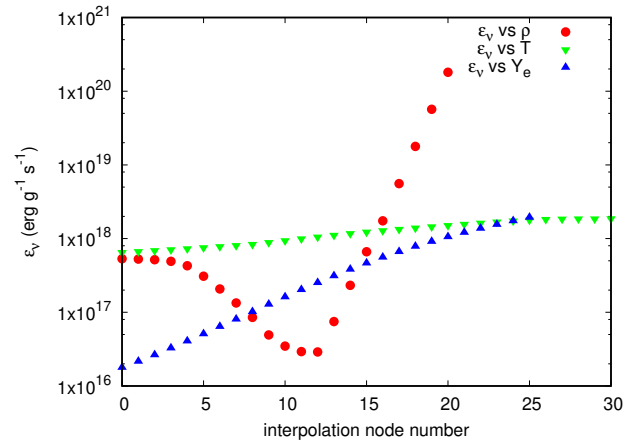


Figure 1. Sample of the variation of the neutrino energy loss-rate as function of density in the range $2 \times 10^5 - 2 \times 10^{10} \text{ g cm}^{-3}$ (at fixed $T = 9 \times 10^9 \text{ K}$ and $Y_e = 0.5 \text{ mol g}^{-1}$, red dots), temperature in the range $3 \times 10^9 - 1.05 \times 10^{10} \text{ K}$ (at fixed $\rho = 2 \times 10^9 \text{ g cm}^{-3}$ and $Y_e = 0.5 \text{ mol g}^{-1}$, green downward triangles), and electron mole number in the range $0.4400 - 0.5025 \text{ mol g}^{-1}$ (at fixed $\rho = 2 \times 10^9 \text{ g cm}^{-3}$ and $T = 9 \times 10^9 \text{ K}$, blue upward triangles) in the interpolation nodes of the NSE table.

- linear interpolation of $\log \dot{Y}_e$ and $\log \varepsilon_{\nu}$ with respect to $\log \rho$ (loglog),
- third order polynomial of the NSE properties, for example \dot{Y}_e , with respect to $\log \rho$ (poly),
- cubic spline fitting the NSE properties with respect to ρ (spline), and
- a physically motivated interpolation function (pevn).

The last interpolator is motivated by the dominant role of protons on the neutronization rate of NSE matter in SNIa models ([Fuller et al. 1985](#); [Brachwitz et al. 2000](#); [Bravo 2019](#)). Then, it seems natural to interpolate using the same function that describes the dependence of the $p(e^-, \nu)n$ rate, or the associated neutrino energy emission-rate, on density ([Fuller et al. 1985](#)). The effective $\log(ft)$ -values characterizing electron captures on protons are almost constant, whereas the rate dependence on ρ is given by the so-called modified phase space factor (Eqs. 3 and 6 in [Fuller et al. 1985](#)), I_e . The neutrino energy emission-rate depends on ρ through the appropriate phase space factor (Eq. 7 in [Fuller et al. 1985](#)), J_e^{ν} . Instead of computing the relativistic Fermi integrals that appear in the definition of these space factors, I calculate approximate values taking advantage of Eqs. 15 in [Fuller et al. \(1985\)](#).

Figures 2 and 3 show the relative error between \dot{Y}_e obtained using the different interpolants and the exact neutronization rate obtained solving the NSE Saha equilibrium equations. The error goes to zero at the table nodes, but can reach up to 1, that is 100% error, at low densities and high temperatures. The dashed lines show the most relevant combination of density and temperature for the SNIa M_{Ch} model in two conditions: when electron captures start on NSE and the neutronization rate is maximum (left columns) and when a value of $Y_e = 0.47 \text{ mol g}^{-1}$ is attained, a condition that is only reached in the innermost $\sim 0.15 M_{\odot}$ of the WD (right columns). The WD mass shells go through ρ - T conditions for which the relative error in \dot{Y}_e is as high as 5–20 % for

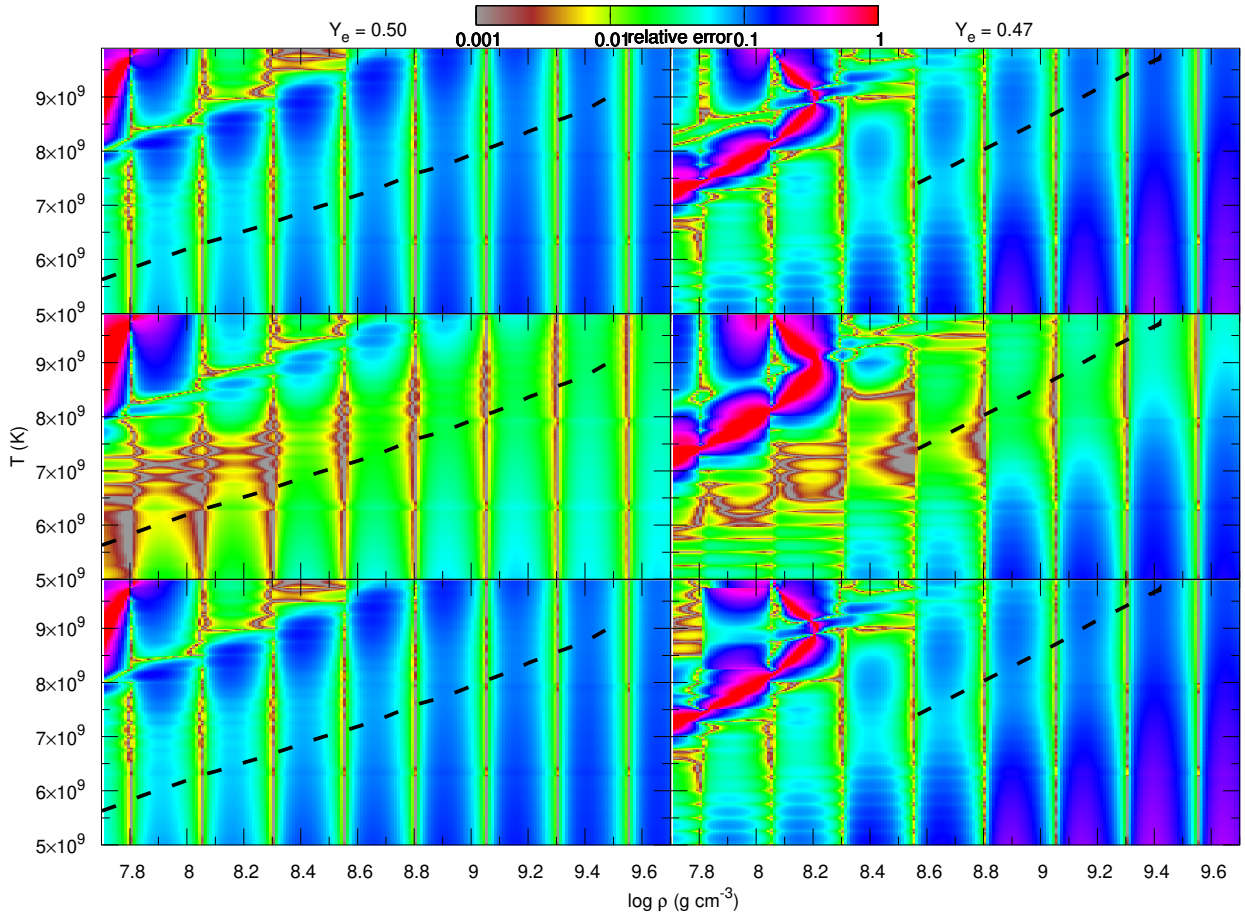


Figure 2. Relative error between the exact neutronization rate, \dot{Y}_e , and that computed by interpolation on a NSE table, for two values of the electron mole number, $Y_e = 0.50 \text{ mol g}^{-1}$ (left column) and $Y_e = 0.47 \text{ mol g}^{-1}$ (right column). The results are shown for different interpolation schemes, from top to bottom: linear interpolation of \dot{Y}_e versus $\log \rho$, linear interpolation of \dot{Y}_e versus ρ , and linear interpolation of $\log \dot{Y}_e$ versus $\log \rho$. The relative error is colour coded according to the colour bar at the top of the plot. The dashed lines show the density and temperature at which the mass shells of model M_{Ch} start experiencing electron captures in NSE (left column) and at the time they reach an electron mole number $Y_e = 0.47 \text{ mol g}^{-1}$ (right column).

the most simple interpolators: linlog, linlin, loglog, and poly. On the other hand, the upper bound to the maximum error in the same conditions is $\sim 3-5\%$ when either the spline or the pevn interpolator is used.

Table 2 shows the impact of the different interpolators on the final yields of the M_{Ch} model, under the heading “NSE table interpolation“. The nucleosynthetic results confirm the intuition gained with Figs. 2 and 3: the most accurate interpolators are the cubic spline and pevn, which perform almost equally well. All interpolants lead to accurate values of the final kinetic energy and just negligible errors in the mass of ^{56}Ni synthesized. The relevant differences appear when one looks into the nucleosynthesis of less abundant species. For instance, using linlog, loglog and poly lead to errors in the ejected mass of ^{57}Ni and ^{55}Fe about 10%, average errors in the isotopic yields of 20–30% (indicator i_6), and order of magnitude errors in the yields of some isotopes with yields smaller than $10^{-3} M_{\odot}$ (indicators i_{13} and i_{14}). On the other hand, the maximum isotopic error obtained with the cubic spline interpolator is 0.8% and that obtained with pevn is

4.2%. The behaviour of interpolator linlin is intermediate between the two groups above.

For simplicity and computational efficiency, in the following tests with simplified networks I have used the cubic spline interpolator for the NSE table.

4 SIMPLIFIED NUCLEAR NETWORKS

Because of the huge difference between the size of a WD and the width of burning waves, multi-dimensional simulations of SNIa need to allocate most memory and CPU resources to solve the hydrodynamic equations in an as large range of length scales as possible (e.g. Gamezo et al. 2003). In turn, the nuclear kinetics must be solved with a reduced nuclear network, with the goal that the nuclear energy must be released as faithfully as possible, as if a complete nuclear network were used. Other compositional properties that affect the equation of state, the electron mole number and the mean molar weight, must also be reproduced accurately in order not to change the explosion development. In this

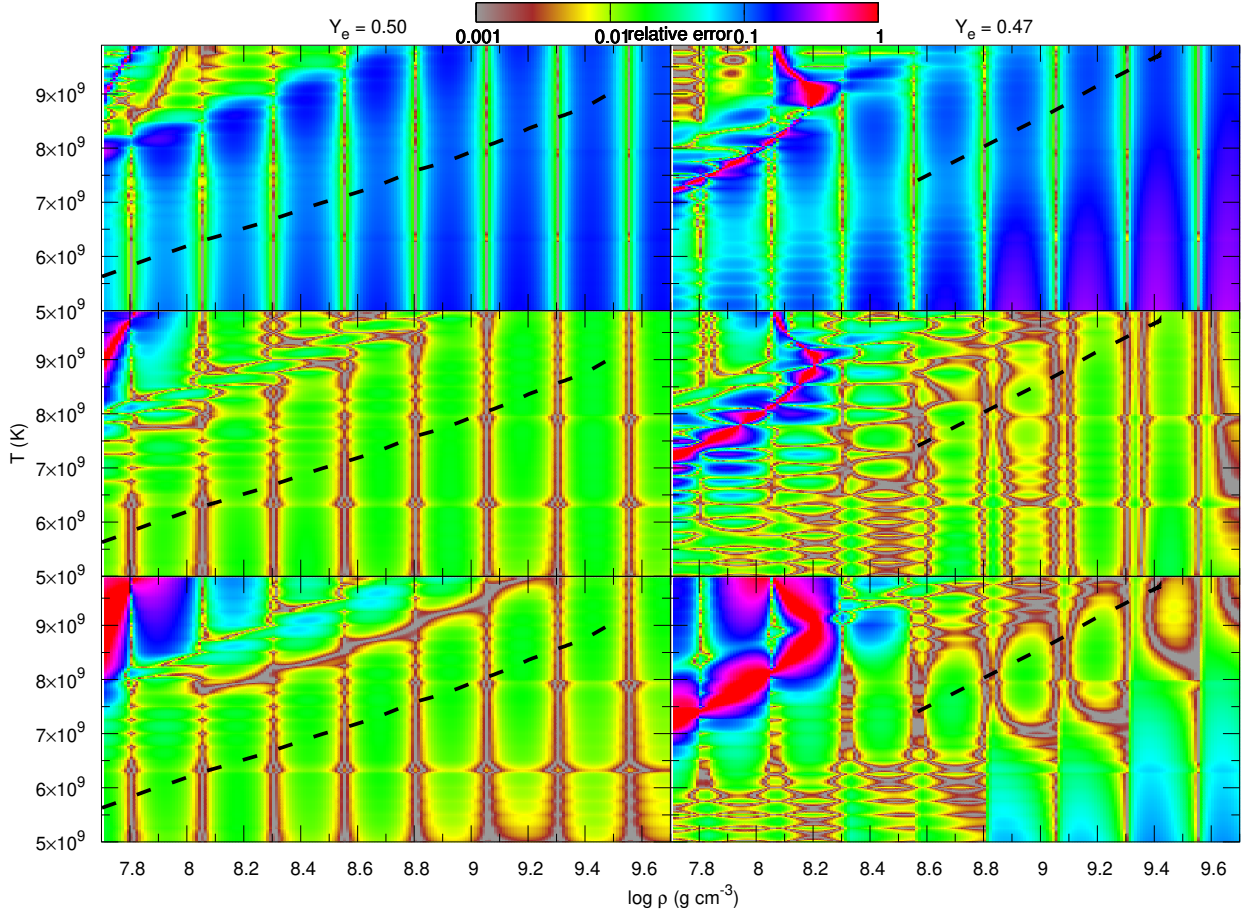


Figure 3. Same as Fig. 2 but for different interpolation schemes, from top to bottom: third order polynomial of \dot{Y}_e versus $\log\rho$, cubic spline of \dot{Y}_e versus ρ , and pevn.

Table 3. Simplified nuclear networks.

Z	iso7	13 α	net21	net23
	A	A	A	A
n	-	-	1	1
p	-	-	1	1
He	4	4	4	4
C	12	12	12	12
O	16	16	16	16
Ne	20	20	20	20,22
Mg	24	24	24	24,25
Si	28	28	28	28
S	-	32	32	32
Ar	-	36	36	36
Ca	-	40	40	40
Ti	-	44	44	44
Cr	-	48	48	48
Fe	-	52	52,53,54, 55,56	52,53,54 55,56
Co	-	-	55,56	55,56
Ni	56	56	56	56

section, I show the impact of the use of reduced nuclear networks on the nucleosynthesis of both the M_{Ch} and the sub- M_{Ch} models in one dimension.

First, I test two small networks, designed iso7 and 13 α , that are widely used in multi-dimensional simulations of SNIa, plus a slightly larger network designed to improve the nucleosynthetic results, named net21. Table 3 shows the composition of each network.

The iso7 network, introduced by Timmes et al. (2000) as a simplification of the nine isotope reaction network described in detail in Table 1 of Woosley (1986), has been used in 2D simulations of DDT models of exploding WDs (e.g. Leung & Nomoto 2018). This network is crafted for efficient computation of nuclear energy generation in multi-dimensional calculations of explosive burning stages from carbon-burning on. It assumes two quasi-equilibrium groups of isotopes, the silicon-group and the iron-group, and hardwires the nucleosynthetic flows between both groups in a single step that link the abundances of ^{28}Si and ^{56}Ni . Timmes et al. (2000) warned that the iso7 and 13 α networks (and, in general, any α -network) might give energy generation rates wrong by order of magnitude if $Y_e \lesssim 0.49 \text{ mol g}^{-1}$.

The 13 α network, introduced by Livne & Arnett (1995) as a simplification of a larger network described in Weaver et al. (1978), has been used in SPH simulations of merging and colliding WDs (Raskin et al. 2014; Dan et al. 2015). The version of the 13 α network used in the present work follows

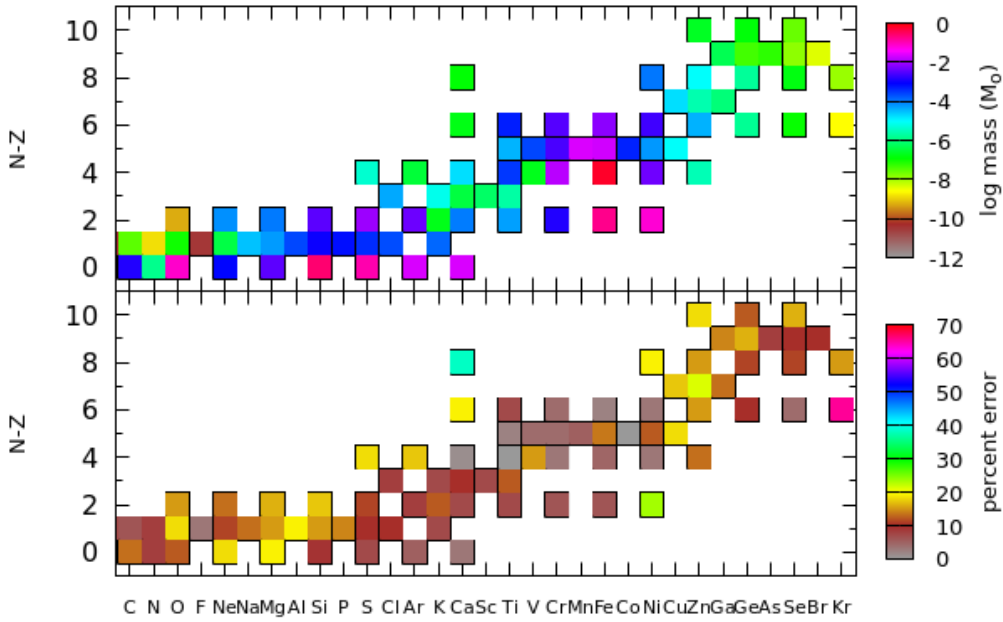
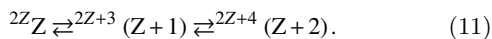


Figure 4. Accuracy of the nucleosynthesis obtained with the net21 network as compared to model ddt2p4_Z6p75e-2_std. **Top:** Final ejected mass of stable isotopes in the reference model. **Bottom:** Percent error of the mass yield of each isotope when the simplified network is used, with respect to the reference model.

Timmes et al. (2000), where it is applied a special treatment to the links between α -nuclei from magnesium on: above a temperature of 2.5×10^9 K, the flows from (α, p) reactions, followed by (p, γ) , are added to the flows from (α, γ) . It is important to note that, in this version of the 13α network³, the link from an α -nucleus, ${}^{2Z}Z$, to the next one, ${}^{2Z+4}(Z+2)$, through (α, p) reactions take into account the possibility that (p, α) follows instead of (p, γ) ,



For instance, in the conversion of ${}^{28}\text{Si}$ into ${}^{32}\text{S}$ through ${}^{31}\text{P}$, the four reactions that follow have to be considered besides ${}^{28}\text{Si}(\alpha, \gamma){}^{32}\text{S}$,



Assuming that the abundance of the intermediate nucleus, ${}^{31}\text{P}$ in this example, is established by the equilibrium of the direct and reverse reactions in Eq. 11, the overall rate of change of the molar fraction of ${}^{2Z+4}(Z+2)$, $Y[{}^{2Z+4}(Z+2)]$, from ${}^{2Z}Z$ is given by,

$$R_{(\alpha, \gamma)}^{\text{eff}} Y[{}^{2Z}Z] Y_{\alpha} - R_{(\gamma, \alpha)}^{\text{eff}} Y[{}^{2Z+4}(Z+2)], \quad (13)$$

where the effective rates, $R_{(\alpha, \gamma)}^{\text{eff}}$ and $R_{(\gamma, \alpha)}^{\text{eff}}$, are:

$$R_{(\alpha, \gamma)}^{\text{eff}} = R_{(\alpha, \gamma)} + R_{(\alpha, p)} \frac{R_{(p, \gamma)}}{R_{(p, \alpha)} + R_{(p, \gamma)}}, \quad (14)$$

and,

$$R_{(\gamma, \alpha)}^{\text{eff}} = R_{(\gamma, \alpha)} + R_{(\gamma, p)} \frac{R_{(p, \alpha)}}{R_{(p, \alpha)} + R_{(p, \gamma)}}, \quad (15)$$

and $R_{(\alpha, p)}$, $R_{(p, \alpha)}$, $R_{(\gamma, p)}$, and $R_{(p, \gamma)}$ are the true rates of the reactions ${}^{2Z}Z \rightarrow {}^{2Z+3}(Z+1)$, ${}^{2Z+3}(Z+1) \rightarrow {}^{2Z}Z$, ${}^{2Z+4}(Z+2) \rightarrow {}^{2Z+3}(Z+1)$, and ${}^{2Z+3}(Z+1) \rightarrow {}^{2Z+4}(Z+2)$, respectively.

In both networks, iso7 and 13α , the electron mole number in the initial model is $Y_e = 0.5 \text{ mol g}^{-1}$. The electron mole number is allowed to change during NSE, due to electron captures, but is kept fixed when the composition is computed by integration of the nuclear network, because it does not include weak interactions.

Table 2 shows the accuracy of the nucleosynthesis obtained post-processing the thermodynamic trajectories belonging to these two networks, under the heading “Simplified networks”. Generally, the performance of the simplified networks in the M_{ch} models is worse than in the sub- M_{Ch} models. The kinetic energy is reasonably reproduced with the simplified networks, slightly better with iso7 than with 13α , and the error in the yield of ${}^{56}\text{Ni}$ is within 6-10% when iso7 is used but it is $\sim 4\%$ with 13α .

The errors in the yields of radioisotopes ${}^{55}\text{Fe}$ and ${}^{57}\text{Ni}$, which are often observationally constrained by the late-time light curves of SNIa, are about 30% with the exception of ${}^{57}\text{Ni}$ in M_{Ch} , whose abundance is wrong by nearly an order of magnitude. These errors are comparable to the maximum deviation obtained in the yields of the most abundant elements, $i_9 \sim 50-60\%$, while the maximum error in the abundance of the isotopes (indicators i_{12} to i_{14}) may be up to several orders of magnitude. Among those with the largest yields, the isotopes that present the maximum deviation are mostly part of the iron group: ${}^{40}\text{Ca}$, ${}^{52,53}\text{Cr}$, ${}^{55}\text{Mn}$, ${}^{57}\text{Fe}$, and ${}^{60,62}\text{Ni}$.

The net21 network is an extension of the 13α network that includes additional isotopes of the iron group plus free

³ See also http://cococubed.asu.edu/code_pages/burn_helium.shtml

protons and neutrons (its full composition can be seen in Table 3), in order to obtain a more reliable representation of the nucleosynthesis of the most deficient nuclides from the results of the iso7 and 13 α networks. Since ^{55}Co is included explicitly in the network, the effective rates between ^{52}Fe and ^{56}Ni given by Eqs. 14 and 15 are substituted by the corresponding true rates, $R_{(\alpha,\gamma)}$ and $R_{(\gamma,\alpha)}$.

When using the net21 network in the hydrocode, the errors in the kinetic energy and the yield of ^{56}Ni after post-processing are about 1–5%. On the other hand, the errors in the yields of ^{55}Fe and ^{57}Ni are less than 7%, and the maximum error in the predicted abundance of any isotope or element is less than 40%, while that of the most abundant isotopes is less than 20% (indicators i_9 and i_{12}).

The errors in the post-processed nucleosynthesis after using the net21 network in the hydrocode are comparable, although slightly larger, than those obtained with the large networks used in the convergence study, netAkh and nse7. Therefore, the performance of net21 would hardly be improved with other simplified network based on no more than a few tenths of nuclides. I have experimented with larger networks, including a group of CNO isotopes ($^{13,14}\text{C}$, ^{14}N , ^{17}O) and the intermediate species in Eq. 11, from ^{27}Al to ^{51}Mn , with no significant improvement in the performance over that of network net21. I have also probed reducing the number of iron group isotopes in the network, but the accuracy of the nucleosynthesis was worse than with net21.

5 NUCLEAR POST-PROCESSING FOR HIGH METALLICITY PROGENITORS

In this section, I test the accuracy of the post-processed nucleosynthesis with respect to the initial metallicity of the progenitor star. The network net21, as well as iso7 and 13 α , is not capable to describe an initial composition of carbon-oxygen material with an excess of neutrons over protons. This is because the initial metallicity of the progenitor star is encoded, at the time of formation of a carbon-oxygen WD, in the abundance of ^{22}Ne (Timmes et al. 2003), which is not a part of any of the simplified networks discussed in the previous section. Then, one may wonder if the accuracy of the net21 network degrades for high metallicity progenitors.

Here, I introduce a new network, net23, that complements the net21 network with the inclusion of ^{22}Ne and ^{25}Mg (Table 3). As just explained, the presence of ^{22}Ne serves the purpose of building initial models with non-zero neutron-excess, as it is done in the hydrodynamic models that use the full network (see Sect. 2). The isotope ^{25}Mg provides a simple route for the burning of ^{22}Ne through $^{22}\text{Ne}(\alpha, n)^{25}\text{Mg}(\alpha, n)^{28}\text{Si}$.

For this test, I have selected an initial metallicity of the WD as high as $Z = 0.0675$. Table 2 shows the results of the post-processed nucleosynthesis using networks net21 and net23, for both the M_{Ch} and the sub- M_{Ch} models, under the heading "High metallicity progenitor". Network net21 performs slightly better in the M_{Ch} model whereas net23 does better in the sub- M_{Ch} model, but the overall accuracy of both networks is similar. When the nucleosynthesis errors in the high metallicity calculations are compared to those in the $Z = 0.009$ models, using the same networks, the results

are slightly better at low metallicity, but not significantly different.

Figure 4 shows the percent error in the prediction of the abundances of the stable isotopes between carbon and krypton after post-processing the thermodynamic trajectories obtained with the net21 network, as compared to those using the default network in the hydrocode. The largest errors belong to ^{48}Ca and ^{78}Kr , whose abundances are below $10^{-6} M_{\odot}$, while all other isotopes are predicted with errors smaller than $\sim 25\%$.

6 TRANSITION FROM THE NUCLEAR NETWORK TO NSE AND VICE VERSA

The simultaneous inclusion in a simulation of a simplified network and an NSE routine, as described in Sect. 3, raises the question of the criteria for the transition between both treatments. The transition between the nuclear network and NSE is usually defined in terms of the temperature, where different values are used for assuming NSE, T_{NSE} , and leaving it, T_{out} . In the hydrocode used in this work, a third parameter, ρ_{NSE0} , allows to accelerate the burning of shells hit by a deflagration front.

Silicon exhaustion is a milestone for achieving NSE. It is reached at a temperature somewhere in between $\sim 5 \times 10^9$ K and $\sim 6 \times 10^9$ K with a slight dependence on ρ (e.g., Fig. 20 in Woosley et al. 1973). In the calculations presented in this section, I have adopted a unified value of T_{NSE} , independent of matter density⁴, as detailed in Table 2.

The freezing-out of nuclear reactions when NSE matter cools is more complex, because at low densities the abundance of free particles (especially α particles) may be sufficiently large to affect significantly the composition. Usual values of the temperature at which matter is assumed to leave NSE lie in the range from $\sim 2 \times 10^9$ K to $\sim 5 \times 10^9$ K. Again, in the calculations presented in this section, there is a single value of T_{out} , independent of density, at variance with the method adopted in the hydrocode using the default network (Bravo et al. 2019).

Following the passage of a deflagrative front, shells are assumed to achieve NSE if their density is larger than a threshold, ρ_{NSE0} . By default, I adopt conservative values for the three parameters: $T_{\text{NSE}} = 6 \times 10^9$ K, $T_{\text{out}} = 5 \times 10^9$ K, and $\rho_{\text{NSE0}} = 8 \times 10^7$ g cm $^{-3}$.

As can be seen in Table 2, the precise value of T_{NSE} does not affect significantly the error of the post-processed nucleosynthesis of the M_{Ch} model, as long as it is in the range from $\sim 5 \times 10^9$ K to $\sim 6 \times 10^9$ K. I recall that the errors reported in this subsection have to be compared with the reference model, that is the net21 M_{Ch} model under the heading "Simplified networks". On the other hand, when the threshold for leaving NSE, T_{out} , takes on a value between 4×10^9 K and 5×10^9 K the accuracy of the nucleosynthesis is satisfactory, but when this parameter goes down to 3×10^9 K the results get worse: for instance, the maximum error in the predicted isotopic yields increases by orders of magnitude. Finally, the accuracy of the nucleosynthesis is not affected by the value

⁴ In the hydrocode using the default network, there are two different values of the minimum temperature to achieve NSE, depending on density, see Bravo et al. (2019) for further details

of ρ_{NSE0} , at least within the range explored in this work and presented in Table 2, $\rho_{\text{NSE0}} = 4 \times 10^7 \text{ g cm}^{-3}$ to 10^8 g cm^{-3} .

7 CONCLUSIONS

Three-dimensional hydrodynamical simulations are necessary to predict the outcome of several explosion scenarios and compare them with SNIa observational data. Whereas great efforts have been made to obtain reliable nucleosynthetic yields and explore their dependence on a number of simulation parameters (e.g. Maeda et al. 2010b; Seitenzahl et al. 2013), until now there have been published very few works addressing the accuracy of the resulting nucleosynthesis with respect to the use of simplified nuclear networks (Papatheodore 2015)⁵. In the present work, I use a supernova code, capable of integrating simultaneously the nuclear kinetic equations using a large nuclear network and the hydrodynamical equations, as a benchmark for testing the results of several simplifying assumptions related to nuclear kinetics. These simplifications are related to the use of a small nuclear network and the use of tabulated properties of matter in nuclear statistical equilibrium. I define a set of fourteen indicators related to the accuracy of the nucleosynthesis.

The method used in this work does not allow testing all the strategies currently used in multi-dimensional simulations of SNIa to follow accurately the nuclear energy generation-rate during a thermonuclear explosion. For instance, several studies (e.g. Travaglio et al. 2004; Dubey et al. 2012; Leung & Nomoto 2017) use Lagrangian tracer particles smartly distributed through the simulated space to advect the thermodynamic properties of the underlying Eulerian cells. The nucleosynthesis is then obtained following a post-processing step on the tracer particles, whose number is much less than the original Eulerian nodes of the simulation. Other studies (e.g. Calder et al. 2007; Fink et al. 2010; Townsley et al. 2016) adopt a nuclear energy generation rate linked to the nature of the burning wave (whether a detonation or a deflagration) and the density of fuel.

I find that the best strategy to incorporate the properties of matter in NSE is to use existing tables of neutronization rate, mean molar number, mean nuclear binding energy, and neutrino energy loss-rate, as functions of density, temperature, and electron molar number, but putting great care in the interpolation between their values at the tabulated density points. The interpolation in temperature and electron mole number is not so critic and can be just linear. A cubic spline interpolation in density gives the most precise results, whose accuracy is better than 1% in all fourteen nucleosynthetic indicators.

The criteria to switch on and off NSE versus integration of the nuclear network are not critical. The temperature at which it can be safely assumed that matter will achieve NSE can adopt any value between $5 \times 10^9 \text{ K}$ and $6 \times 10^9 \text{ K}$. Once a layer achieves the NSE state, it can be maintained for temperatures in excess of $\sim 4 \times 10^9 \text{ K}$. But, if the NSE state is kept until a temperature as low as $3 \times 10^9 \text{ K}$, the resulting

post-processed nucleosynthesis can be orders of magnitude wrong even for isotopes whose yield is $> 10^{-3} M_{\odot}$.

I tested several simplified nuclear networks for the accuracy of the nucleosynthesis obtained after post-processing, compared with the nucleosynthesis resulting directly from the supernova code when the default, large, nuclear network is used. Short networks (iso7 and 13 α) are able to give an accurate yield of ^{56}Ni , after post-processing, but can fail by order of magnitude predicting the ejected mass of even mildly abundant species ($> 10^{-3} M_{\odot}$). I find that a network of 21 species reproduces nicely the nucleosynthesis of Chandrasekhar and sub-Chandrasekhar explosions, their average errors being better than 10% for the most abundant elements and isotopes (yields larger than $10^{-3} M_{\odot}$) and better than 20% for the whole set of stable elements and isotopes followed in the model.

ACKNOWLEDGEMENTS

This work has been supported by the MINECO-FEDER grants AYA2015-63588-P and PGC2018-095317-B-C21.

REFERENCES

- Arsenijevic V., Fabbro S., Mourão A. M., Rica da Silva A. J., 2008, *A&A*, **492**, 535
- Badenes C., Borkowski K. J., Hughes J. P., Hwang U., Bravo E., 2006, *ApJ*, **645**, 1373
- Blondin S., Dessart L., Hillier D. J., Khokhlov A. M., 2013, *MNRAS*, **429**, 2127
- Blondin S., Dessart L., Hillier D. J., Khokhlov A. M., 2017, *MNRAS*, **470**, 157
- Brachwitz F., et al., 2000, *ApJ*, **536**, 934
- Branch D., Fisher A., Nugent P., 1993, *AJ*, **106**, 2383
- Branch D., Chau Dang L., Baron E., 2009, *PASP*, **121**, 238
- Bravo E., 2019, *A&A*, **624**, A139
- Bravo E., García-Senz D., 2006, *ApJ*, **642**, L157
- Bravo E., Martínez-Pinedo G., 2012, *Phys. Rev. C*, **85**, 055805
- Bravo E., Domínguez I., Badenes C., Piersanti L., Straniero O., 2010, *ApJ*, **711**, L66
- Bravo E., Badenes C., Martínez-Rodríguez H., 2019, *MNRAS*, **482**, 4346
- Calder A. C., et al., 2007, *ApJ*, **656**, 313
- Churazov E., et al., 2014, *Nature*, **512**, 406
- Churazov E., et al., 2015, *ApJ*, **812**, 62
- Cyburtt R. H., et al., 2010, *ApJS*, **189**, 240
- Dan M., Guillochon J., Brügggen M., Ramirez-Ruiz E., Rosswog S., 2015, *MNRAS*, **454**, 4411
- Diehl R., et al., 2014, *Science*, **345**, 1162
- Dimitriadis G., et al., 2017, *MNRAS*, **468**, 3798
- Dubey A., Daley C., Zuhone J., Ricker P. M., Weide K., Graziani C., 2012, *ApJS*, **201**, 27
- Filippenko A. V., 1997, *ARA&A*, **35**, 309
- Fink M., Röpké F. K., Hillebrandt W., Seitenzahl I. R., Sim S. A., Kromer M., 2010, *A&A*, **514**, A53+
- Fuller G. M., Fowler W. A., Newman M. J., 1985, *ApJ*, **293**, 1
- Gamezo V. N., Khokhlov A. M., Oran E. S., Chtchelkanova A. Y., Rosenberg R. O., 2003, *Science*, **299**, 77
- Graur O., Zurek D., Shara M. M., Riess A. G., Seitenzahl I. R., Rest A., 2016, *ApJ*, **819**, 31
- Graur O., et al., 2018, *ApJ*, **859**, 79
- Hillebrandt W., Niemeyer J. C., 2000, *Annual Review of Astronomy and Astrophysics*, **38**, 191
- Hoeflich P., et al., 2017, preprint, ([arXiv:1707.05350](https://arxiv.org/abs/1707.05350))

⁵ https://trace.tennessee.edu/utk_graddiss/3454/

- Höflich P., Khokhlov A., 1996, *ApJ*, **457**, 500
- Hosseinzadeh G., et al., 2017, *ApJ*, **845**, L11
- Howell D. A., 2011, *Nature Communications*, **2**, 350
- Howell D. A., Höflich P., Wang L., Wheeler J. C., 2001, *ApJ*, **556**, 302
- Howell D. A., et al., 2005, *ApJ*, **634**, 1190
- Isern J., et al., 2016, *A&A*, **588**, A67
- Jacobson-Galán W. V., Dimitriadis G., Foley R. J., Kilpatrick C. D., 2018, *ApJ*, **857**, 88
- James J. B., Davis T. M., Schmidt B. P., Kim A. G., 2006, *MNRAS*, **370**, 933
- Kasen D., Woosley S. E., 2007, *ApJ*, **656**, 661
- Katz B., Dong S., 2012, arXiv e-prints, p. [arXiv:1211.4584](https://arxiv.org/abs/1211.4584)
- Khokhlov A. M., 1991, *A&A*, **245**, 114
- Kushnir D., 2019, *MNRAS*, **483**, 425
- Kushnir D., Katz B., Dong S., Livne E., Fernández R., 2013, *ApJ*, **778**, L37
- Leung S.-C., Nomoto K., 2017, preprint, ([arXiv:1710.04254](https://arxiv.org/abs/1710.04254))
- Leung S.-C., Nomoto K., 2018, *ApJ*, **861**, 143
- Li W., et al., 2019, arXiv e-prints, p. [arXiv:1906.07321](https://arxiv.org/abs/1906.07321)
- Livne E., Arnett D., 1995, *ApJ*, **452**, 62
- Lopez L. A., Ramirez-Ruiz E., Huppenkothen D., Badenes C., Pooley D. A., 2011, *ApJ*, **732**, 114
- Maeda K., et al., 2010a, *Nature*, **466**, 82
- Maeda K., Röpke F. K., Fink M., Hillebrandt W., Travaglio C., Thielemann F., 2010b, *ApJ*, **712**, 624
- Maguire K., et al., 2018, *MNRAS*, **477**, 3567
- Maoz D., Mannucci F., Nelemans G., 2014, *Annual Review of Astronomy and Astrophysics*, **52**, 107
- Martínez-Rodríguez H., et al., 2018, *ApJ*, **865**, 151
- Maund J. R., et al., 2010, *ApJ*, **725**, L167
- Maund J. R., et al., 2013, *MNRAS*, **433**, L20
- Miller A. A., et al., 2018, *ApJ*, **852**, 100
- Nugent P., Baron E., Branch D., Fisher A., Hauschildt P. H., 1997, *ApJ*, **485**, 812
- Papatheodore T. L., 2015, PhD thesis, University of Tennessee, Knoxville
- Parikh A., José J., Seitenzahl I. R., Röpke F. K., 2013, *A&A*, **557**, A3
- Plewa T., Calder A. C., Lamb D. Q., 2004, *ApJ*, **612**, L37
- Poznanski D., Gal-Yam A., Maoz D., Filippenko A. V., Leonard D. C., Matheson T., 2002, *PASP*, **114**, 833
- Raskin C., Kasen D., Moll R., Schwab J., Woosley S., 2014, *ApJ*, **788**, 75
- Röpke F. K., Hillebrandt W., Niemeyer J. C., Woosley S. E., 2006, *A&A*, **448**, 1
- Scalzo R., et al., 2014, *MNRAS*, **440**, 1498
- Seitenzahl I. R., Townsley D. M., Peng F., Truran J. W., 2009, *Atomic Data and Nuclear Data Tables*, **95**, 96
- Seitenzahl I. R., et al., 2013, *MNRAS*, **429**, 1156
- Shappee B. J., Stanek K. Z., Kochanek C. S., Garnavich P. M., 2017, *ApJ*, **841**, 48
- Sim S. A., Röpke F. K., Hillebrandt W., Kromer M., Pakmor R., Fink M., Ruiter A. J., Seitenzahl I. R., 2010, *ApJ*, **714**, L52
- Stritzinger M., Mazzali P. A., Sollerman J., Benetti S., 2006, *A&A*, **460**, 793
- Tanaka M., Mazzali P. A., Stanishev V., Maurer I., Kerzendorf W. E., Nomoto K., 2011, *MNRAS*, **410**, 1725
- Thielemann F.-K., Nomoto K., Yokoi K., 1986, *A&A*, **158**, 17
- Timmes F. X., Hoffman R. D., Woosley S. E., 2000, *ApJS*, **129**, 377
- Timmes F. X., Brown E. F., Truran J. W., 2003, *ApJ*, **590**, L83
- Townsley D. M., Miles B. J., Timmes F. X., Calder A. C., Brown E. F., 2016, *ApJS*, **225**, 3
- Travaglio C., Hillebrandt W., Reinecke M., Thielemann F. K., 2004, *A&A*, **425**, 1029
- Wang L., Wheeler J. C., Li Z., Clocchiatti A., 1996, *ApJ*, **467**, 435
- Weaver T. A., Zimmerman G. B., Woosley S. E., 1978, *ApJ*, **225**, 1021
- Woosley S. E., 1986, in Audouze J., Chiosi C., Woosley S. E., eds, Saas-Fee Advanced Course 16: Nucleosynthesis and Chemical Evolution. p. 1
- Woosley S. E., Kasen D., 2010, preprint, ([arXiv:1010.5292](https://arxiv.org/abs/1010.5292))
- Woosley S. E., Weaver T. A., 1994, *ApJ*, **423**, 371
- Woosley S. E., Arnett W. D., Clayton D. D., 1973, *ApJS*, **26**, 231
- Yang Y., et al., 2018, *ApJ*, **852**, 89
- Zheng W., et al., 2013, *ApJ*, **778**, L15

This paper has been typeset from a $\text{\TeX}/\text{\LaTeX}$ file prepared by the author.